Atmos. Meas. Tech., 9, 4151–4165, 2016
www.atmos-meas-tech.net/9/4151/2016/
doi:10.5194/amt-9-4151-2016

Atmospheric Measurement Techniques Open Access EGU

Coupling sky images with radiative transfer models: a new method to estimate cloud optical depth

Felipe A. Mejia, Ben Kurtz, Keenan Murray, Laura M. Hinkelman, Manajit Sengupta, Yu Xie, and Jan Kleissl

Center for Renewable Resources and Integration, Department of Mechanical and Aerospace Engineering, University of California, San Diego 9500 Gilman Dr., La Jolla, CA 92093, USA

Correspondence to: Felipe A. Mejia (famejia@ucsd.edu)

Received: 9 September 2015 – Published in Atmos. Meas. Tech. Discuss.: 30 October 2015
Revised: 26 May 2016 – Accepted: 29 June 2016 – Published: 30 August 2016

Abstract. A method for retrieving cloud optical depth (τ_c) using a UCSD developed ground-based sky imager (USI) is presented. The radiance red–blue ratio (RRBR) method is motivated from the analysis of simulated images of various τ_c produced by a radiative transfer model (RTM). From these images the basic parameters affecting the radiance and red–blue ratio (RBR) of a pixel are identified as the solar zenith angle (θ_0), τ_c, solar pixel angle/scattering angle (ϑ_s), and pixel zenith angle/view angle (ϑ_z). The effects of these parameters are described and the functions for radiance, $I_\lambda(\tau_c, \theta_0, \vartheta_s, \vartheta_z)$, and $\mathrm{RBR}(\tau_c, \theta_0, \vartheta_s, \vartheta_z)$ are retrieved from the RTM results. RBR, which is commonly used for cloud detection in sky images, provides non-unique solutions for τ_c, where RBR increases with τ_c up to about $\tau_c = 1$ (depending on other parameters) and then decreases. Therefore, the RRBR algorithm uses the measured $I_\lambda^{\mathrm{meas}}(\vartheta_s, \vartheta_z)$, in addition to $\mathrm{RBR}^{\mathrm{meas}}(\vartheta_s, \vartheta_z)$, to obtain a unique solution for τ_c. The RRBR method is applied to images of liquid water clouds taken by a USI at the Oklahoma Atmospheric Radiation Measurement (ARM) program site over the course of 220 days and compared against measurements from a microwave radiometer (MWR) and output from the Min et al. (2003) method for overcast skies. τ_c values ranged from 0 to 80 with values over 80, being capped and registered as 80. A τ_c RMSE of 2.5 between the Min et al. (2003) method and the USI are observed. The MWR and USI have an RMSE of 2.2, which is well within the uncertainty of the MWR. The procedure developed here provides a foundation to test and develop other cloud detection algorithms.

1 Introduction

Advances in solar photovoltaic (PV) technologies have paved the way for higher PV penetration but as we rely more heavily on solar energy it becomes ever more crucial to understand the characteristics of this energy source. Unlike fossil fuels, solar energy has an inherent variability that causes difficulty when integrating solar energy into the grid. Improving forecasting of the available solar irradiance will support management of the electric grid and electricity markets and therefore ensure a more economical integration of solar power (Mathiesen et al., 2013). Currently several different methods are used to forecast at different spatial and temporal resolutions including numerical weather prediction (e.g., Lorenz et al., 2009; Mathiesen and Kleissl, 2011) and satellite image-based forecasting (e.g., Hammer et al., 1999). For short-term forecasting, whole-sky imagery has been used (e.g., Urquhart et al., 2013).

Physics-based solar forecasting using whole-sky imagery requires geolocating clouds in the sky images, estimating their optical depth, motion, and dynamics (Chow et al., 2011). To estimate a cloud's optical depth (τ_c), the most advanced methods separate the image into clear sky, thin cloud, and thick cloud and assign a τ_c to each of these groups. To distinguish thin and thick clouds, the red–blue ratio (RBR) (or a function of RBR) has been used as the default method (Koehler et al., 1991; Shields et al., 1993; Chow et al., 2011; Ghonima et al., 2012; Roy et al., 2001). It is defined as the ratio of the signal from the red channel to the signal from the blue channel. The RBR method takes advantage of Rayleigh scattering being greater in the blue wavelengths than the red wavelengths. When Rayleigh scattering is the predominant form of scattering, such as in clear skies, the RBR for a given

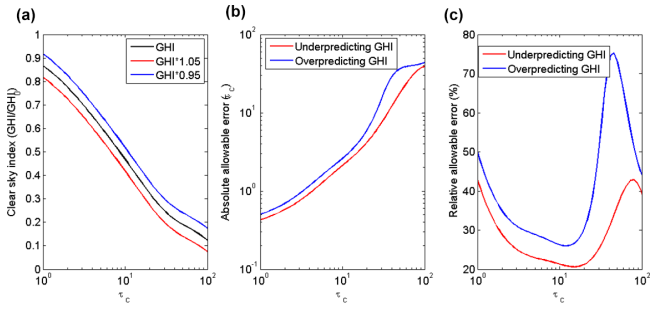

Figure 1. **(a)** GHI divided by clear-sky GHI as a function of τ_c for homogenous clouds as derived from SHDOM. The black line represents the results while the blue and red are 5 % offsets in clear-sky GHI. **(b)** Error bounds of ±5 % clear-sky GHI in **(a)** converted to absolute intervals for τ_c. For example, for GHI to stay within 5 % clear-sky GHI at $\tau_c = 30$, τ_c cannot be more than 7.7 below 30 and not more than 15.6 above 30. **(c)** Same as **(b)** but the y axis is divided by τ_c.

view angle is smaller than under cloud scattering. RBR successfully differentiates clear sky from thin clouds and to a more limited extent thick clouds, but the RBR has not been applied to differentiate τ_c. It is also difficult to apply the RBR method in the circumsolar region as thick dark clouds have lower RBRs than clear sky (Chow et al., 2011). In fact we will demonstrate in this paper through radiative transfer modeling (Sect. 4) that RBR by itself is ineffective for differentiating τ_c even for homogeneous cloud layers.

Differences in τ_c can greatly affect the irradiance available for solar energy production. For solar power integration into the markets the impacts of forecast errors at individual plants can be considered to scale linearly with forecast error. Any kW of power not produced at solar power plant A will have to be provided by another dispatchable generator B and, depending on market rules, will result in economic losses for the solar power plant. For this analysis we consider the accuracy requirement of global horizontal irradiance (GHI) to be ±5 % of clear-sky GHI (Fig. 1a). Figure 1b and c demonstrate the corresponding absolute and relative error in τ_c for a 5 % error of the clear-sky GHI. Relative τ_c accuracy required for solar forecasting is large for thin clouds ($\tau_c \sim 1$) and thick clouds ($\tau_c > 30$). A minimum occurs at $\tau_c = 16$, where a 21 % error in τ_c is permissible for avoiding an underprediction of GHI by 5 % of the clear-sky value. PV power production is a close to linear function of global irradiance. Therefore Fig. 1a expresses effects of cloud optical depth on PV power production. Even at $\tau_c = 100$ PV power output is still at over 10 % of clear-sky conditions, which is still important for solar energy production.

Most current cloud detection methods are designed empirically using lookup tables and/or thresholds that are adjusted to "work" with a specific imager and cloud conditions (see Sect. 2). The present paper breaks new ground in that it attempts to improve our fundamental understanding of the impact of radiative transfer (RT) and τ_c on the radiance and RBR of a given pixel in a sky image. To analyze this relation, the spherical harmonic discrete ordinate method (SHDOM) (Evans, 1998; Pincus and Evans, 2009) is used to produce synthetic overcast sky images (Sect. 3) and analyze the determinants of sky imager (USI) radiances (Sect. 4). The results reveal nonlinearities and non-monotonic behavior in radiances and RBR that explain many of the challenges previously observed with empirical cloud detection methods. The insights gained through RT are utilized to develop a τ_c retrieval algorithm for sky imagery (Sect. 5). The algorithm is compared to other methods in Sect. 6 and a discussion and conclusions are presented in Sect. 7.

2 Review of sky imager cloud detection methods and geometrical factors

Individual pixel cloud detection using the output image from sky imagers is based on either the radiance measurement or the ratio between radiance measurements for different wavelengths. Cloud detection algorithms using single channel radiance have found limited success (McGuffe et al., 1989; Kegelmeyer, 1994) due to the similarities in radiance values between clear skies and thick clouds in the visible spectrum. More success has been obtained when cloud detection uses the ratio between radiance measurements at different wavelength bands. One such algorithm is the RBR method, which uses the ratio of camera measurement in the red channel to the blue channel to classify a pixel as cloudy or clear. A fixed RBR threshold between clear sky and cloudy sky (Koehler et al., 1991) led to successful identification of opaque clouds but consistently failed to distinguish thin and clear skies. However, in a study of contrail clouds, Koehler et al. (1991) observed that the ratio of RBR to the clear-sky RBR was similar between contrail cases and motivated a method for identifying thin clouds. In other words, knowing the clear-sky background value aids in the detection of thin clouds. The main factors affecting the clear-sky RBR were found to be the solar zenith angle (θ_0), solar pixel angle/scattering angle (ϑ_s), pixel zenith angle/view angle (ϑ_z, see Figs. 2, 3b, c for illustrations of these angles), and changes in aerosol properties. This lead to the development of clear-sky libraries (CSL) (Shields et al., 1993; Chow et al., 2011) to express clear-sky RBR values under any condition. CSL are constructed by binning pixel values from clear-sky images into matrices as a function of θ_0 (Fig. 2), ϑ_s, and ϑ_z. From the CSL it is then possible to simulate a clear sky (Fig. 3a) for any given day, allowing the calculation of the ratio of measured RBR to clear-sky RBR.

The red–blue difference (RBD; Heinle et al., 2010) uses the same principles as the RBR for cloud detection but attempts to mitigate the strong directional variability in the RBR due to variability in the radiance, $I_{\Delta\lambda}$, of the blue chan-

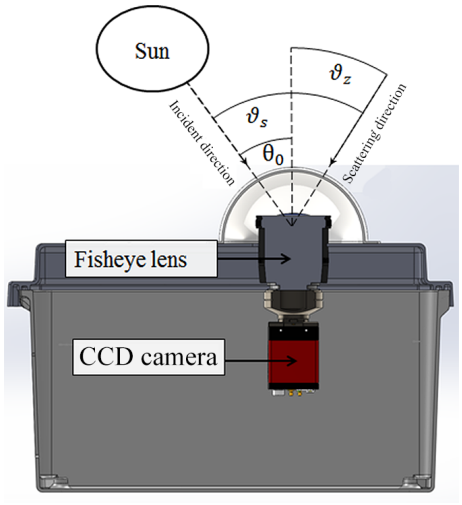

Figure 2. Diagram of the UCSD sky imager (USI) and related solar and sky geometries. θ_0 is the solar zenith angle. The ϑ_s is the angle subtended by the vector pointing at the sun and the vector pointing at the pixel in question. The ϑ_z is the angle formed by the vector pointing at the pixel in question and zenith. It is important to note that $\vartheta_s = \theta_0 + \vartheta_z$ only holds in 2-D but not in 3-D because the incident and scattering directions may not be in the same azimuthal plane. An example of this is illustrated in Fig. 3.

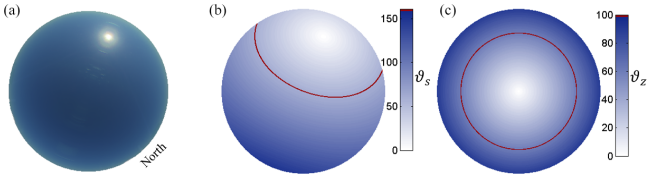

Figure 3. (a) Clear USI image created from a clear-sky library for a solar zenith angle of 60° on 26 March 2013, 15:00:00 UTC. For the image in **(a)** solar pixel angles and pixel zenith angles are shown in **(b)** and **(c)**, respectively. The red lines in **(b)** and **(c)** highlight the pixels with $\vartheta_s = 60°$ and $\vartheta_z = 60°$, respectively, which are often used in the following chapters to illustrate relationships with cloud optical depth and radiance. North is located on the bottom right corner of the image.

nel as seen in Eqs. (1, 2):

$$\mathrm{RBR} = \frac{I_r}{I_b} = 1 + \frac{I_r - I_b}{I_b}, \quad (1)$$

$$\mathrm{RBD} = I_r - I_b = I_b(\mathrm{RBR} - 1), \quad (2)$$

where I_r is the $I_{\Delta\lambda}$ in the red channel, and I_b is the $I_{\Delta\lambda}$ in the blue channel. However, Ghonima et al. (2012) found minimal differences in performance between RBD and RBR retrieval with RBR outperforming RBD. Gauchet et al. (2012) used RBD combined with a different approach to account for the directional effects in cloud detection, in which they segmented images into five zones, solar disk, circumsolar disk, extended circumsolar disk, main zone, sky horizon, and orographic horizon. The radiance and RBD thresholds to separate clear sky, bright cloud, and dark cloud varied by zone.

These approaches have led to improved accuracy of cloud detection, yet limited progress has been made towards understanding the phenomena that influence the performance of these methods. Although a direct relationship with aerosol optical depth (τ_a) and RBR is observed for small τ_a, ($\tau_a < 0.3$) (Ghonima et al., 2012) no direct relationship has been found between RBR, or other variables determined from sky imagers, and larger optical depths ($\tau > 0.3$) such as those found typically in clouds. This has limited sky imager cloud detection to a binary classification in which the image is segmented into cloud or clear sky. The lack of research on τ_c classification also stems from the fact that τ_c is challenging to measure accurately and large spatio-temporal variability. Instead, a radiative transfer model is applied here to investigate the interrelationships between radiances, radiance ratios (RBR), and τ_c and to devise a method to detect τ_c.

3 Radiative transfer modeling of sky images and comparison to measurements

3.1 SHDOM model and input parameters

Radiance measurements can be obtained from a 1-D model for homogeneous clouds but in anticipation of future work a 3-D RT model was used. SHDOM is an explicit 3-D RT model that uses discrete ordinates to integrate the radiative transfer equation spatially, while spherical harmonics are used to save memory when computing scattering. SHDOM is more computationally efficient compared to Monte Carlo (MC) methods when solving the whole-sky radiance field. SHDOM is also found to be within 2–3 % (close to the noise level) of the MC models in the intercomparison of 3-D radiation codes (I3RC) (Marshak and Davis, 2005; Cahalan et al., 2005). Because of its computational efficiency and accuracy, SHDOM is selected for this analysis. SHDOM radiative transfer calculations are performed for 161 liquid water overcast skies with homogeneous τ_c, ranging in τ_c from 0 to 80 at solar zenith angles ranging from 21 to 70° and for wavelengths corresponding to the peaks of the USI camera's red (620 nm), green (520 nm), and blue (450 nm) channels.

To calculate the single scattering properties of aerosols in the SHDOM simulation such as aerosol effective radius and refractive index, yearly average AERosol RObotic NETwork (AERONET) data from the Atmospheric Radiation Measurement (ARM) Southern Great Plains (SGP) site for the year of 2013 are used (Holben et al., 1998, 2001) (Table 1). Background Rayleigh and aerosol optical depths are also obtained from yearly averages taken from the sun-tracking photometer at the ARM SGP site. Spectral surface reflectances of 0.043, 0.068, and 0.071 were used for the blue, green, and red channel simulations, respectively (Marchand et al., 2004). A cloud droplet effective radius of 8 µm (Min et al., 2003) is

Table 1. Atmospheric radiative properties for the ARM site used as input to SHDOM. τ_a and Rayleigh optical depth are averages for the year 2013 from AERONET data.

	Red (620 nm)	Green (520 nm)	Blue (450 nm)
τ_a [–]	0.0784	0.1010	0.1212
Rayleigh optical depth [–]	0.0875	0.1627	0.2296
Aerosol effective radius (R_e) [µm]	3.9	3.9	3.9
Aerosol R_e distribution	Lognormal	Lognormal	Lognormal
Refractive index [–]	1.42–0.002i	1.41–0.002i	1.40–0.002i

used to obtain the single scattering properties of the clouds in the SHDOM simulations. Given the desired τ_c, cloud liquid water content (LWC) for input to SHDOM is computed as (Stephens, 1978)

$$\mathrm{LWC} \approx \frac{\frac{2}{3}\,\tau_c\,\rho_l r_e}{\Delta z}, \tag{3}$$

where ρ_l is the density of liquid water and Δz is the cloud geometric thickness. In this study, LWC is assumed constant between a cloud base of 1 km and cloud top of 2 km, giving a Δz of 1 km.

The SHDOM output radiance field is used to reproduce a sky image that would be obtained through a fisheye lens with an equisolid angle projection (Miyamoto, 1964):

$$r' = 2f \sin\left(\frac{\vartheta_z}{2}\right), \tag{4}$$

where f is the focal length, and r' is the distance from the principal point in the image plane.

3.2 USI hardware and calibration of the signal to radiance

On 14 March 2013 we deployed two USIs (serial numbers 1.7 and 1.8) at the ARM SGP site. The instrument domes were cleaned weekly. Daytime images from the USIs were collected continuously every 30 s for 220 days. Since USI 1.8 was located closer (at 200 m distance) to the instruments used for comparison, it is used for the analysis. The optical setup included a Sigma 4.5 mm fisheye lens, an infrared filter, and an Allied Vision GE2040 CCD camera (Fig. 2). The fisheye lens creates an equisolid angle projection onto the CCD, resulting in an image where the solid angle subtended on each CCD cell (pixel) is approximately constant. Custom apertures were inserted into the lens of both USIs with diameters of 700 and 1000 µm for USI 1.7 and 1.8, respectively. A Bayer color filter on the CCD separates pixels into red, green, and blue pixels allowing for multispectral images. Three different images are taken at different exposure times and combined to create a high dynamic range image (Urquhart et al., 2015). The signal measured by each pixel is related to the amount of photons that are transmitted through the optics and converted to a voltage. The signal measured can therefore be calibrated to estimate the irradiance, $E_{\Delta\lambda}$ at a wavelength band, incident on a pixel. The radiance $I_{\Delta\lambda}^{\mathrm{meas}}$ observed by each pixel can then be calculated using

$$I_{\Delta}\lambda^{\mathrm{meas}} = \frac{E_{\Delta\lambda}}{\Delta\Omega\Delta\lambda} = \frac{C_{1_\lambda}\cdot v}{\Delta t\, A_{\mathrm{in}}\Delta\Omega\Delta\lambda} = C_{2_\lambda}\cdot v, \tag{5}$$

where v is the camera measurement in counts at a given pixel, C_{1_λ} (units of J count^{-1}) is a calibration factor between v and $E_{\Delta\lambda}\Delta t\, A_{\mathrm{in}}$, C_{2_λ} (units of W m^{-2} st^{-1} nm^{-1} count^{-1}) is a calibration factor between v and $I_{\Delta\lambda}^{\mathrm{meas}}$, A_{in} is the area of the pixel, $\Delta\Omega$ is the solid angle, and $\Delta\lambda$ is the wavelength band. Given the equisolid angle lens, A_{in}, $\Delta\Omega$, and $\Delta\lambda$ are assumed constant across the image sensor, resulting in a linear relationship (after correcting optical errors as shown in the Appendix and camera sensor nonlinearities which are negligible for our camera as seen in Fig. 4) between the camera signal v and the radiance $I_{\Delta\lambda}$ at the pixel's ϑ_z as

$$C_{2_\lambda} = \frac{\overline{I_{\Delta\lambda}(\vartheta_z, \vartheta_s)}}{\overline{v(\vartheta_z, \vartheta_s)}}. \tag{6}$$

The calibration constant C_{2_λ} is obtained as the average (denoted as overbar in Eq. 6) of 131 overcast (cloud fraction (CF) is greater than 0.9) images on 98 different days. Overcast skies are preferred because the radiance is more homogeneous and since the method by Min et al. (2003) could be applied to obtain the τ_c that is input to SHDOM. C_{2_λ} values are 1.16×10^{-4} , 1.11×10^{-4}, and 9.69×10^{-5} W m^{-2} st^{-1} nm^{-1} for the red, green, and blue channels, respectively. Figure 4 demonstrates the three signal calibrations with a relative root mean square error (RMSE) of 0.155, 0.148, and 0.144 for the red, green, and blue channel respectively. This RMSE is within the range of the radiance variability expected in overcast clouds (Szczodrak et al., 2001). Field calibration to modeled SHDOM data was preferred here as lab calibrations of sky imagers are rarely available. Therefore the calibration method presented here is more widely applicable and provides a calibration that is consistent with the Min et al. (2003) method. Validation of the field calibration with independent lab calibration is left for future work.

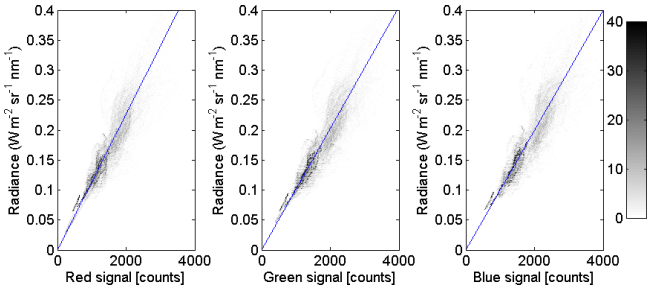

Figure 4. SHDOM radiance ($I_{\Delta\lambda}(\vartheta_z, \vartheta_s)$) vs. USI pixel signal value ($v(\vartheta_z, \vartheta_s)$). Dots with grayscale indicate density while the blue line is the best fit line.

3.3 Application to other imaging systems

Other ground-based sky imaging designs have also been developed (Seiz et al., 2007; Souza-Echer et al., 2006; Calbo and Sabburg, 2008; Cazorla et al., 2008; Heinle et al., 2010; Román et al., 2012; Gauchet et al., 2012) with the most dissimilar design consisting of a downward-pointing camera capturing the sky from a reflection off a spherical mirror (Pfister et al., 2003; Kassianov et al., 2005; Long et al., 2006; Mantelli et al., 2010; Martínez-Chico et al., 2011). Most ground imaging devices follow a relationship between the camera's signal and radiance similar to Eq. (5), differing only in the wavelength region $\Delta\lambda$, calibration factors C_{1_λ}, and C_{2_λ} and optical and sensor errors, with non-equisolid lens camera systems requiring $\Delta\Omega$ to be specified per pixel. Therefore the method presented here can be adapted easily to images from other sky imaging systems.

3.4 Comparison of real and synthetic (SHDOM) images and stray light correction

Example measured images and their SHDOM equivalent images are illustrated in Fig. 5. Differences between the clear-sky image (Fig. 5a) and the synthetic image (Fig. 5b) highlight the impacts of stray light as well as the vertical smear stripe caused by the CCD sensor (Fig. 5c). The stray light is particularly strong in the circumsolar region causing enhancement of the red radiance of up to 50 %. Stray light is caused by light from the direct beam being scattered through the optics (mainly the protective acrylic dome). This means that stray light is strongest for $\tau_c = 0$ and should decrease to 0 once clouds are thick enough to eliminate the direct beam, which occurs at roughly $5 < \tau_c < 12$, depending on the solar zenith angle. Particular optical reflections are observed as circular patterns throughout the image that are aligned with the solar azimuth. While stray light patterns are often consistent for the same sun position, misalignments in the camera optics (e.g., during instrument maintenance) can lead to stray light changing under constant ϑ_s and ϑ_z, making it difficult to implement a general stray light correction, for example through a lookup table. Stray light leads to brighter pixel values than

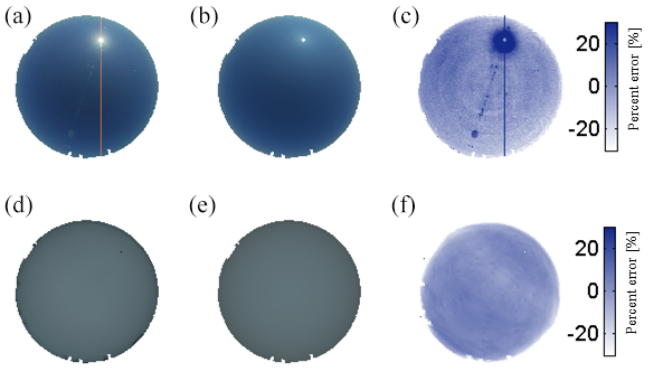

Figure 5. **(a)** Clear-sky USI image for 26 March 2013, 15:00:00 UTC; **(b)** synthetic image from SHDOM for τ_c of 0 and θ_0 of 60°; **(c)** percent error in red channel radiance; **(d)** USI image for 5 May 2013, 14:08:00 UTC; **(e)** synthetic image for θ_0 of 60° and τ_c of 30; **(f)** percent error in red channel radiance.

expected, which in turn can lead to misclassifications of clear sky as thin clouds (in the range $0 < \tau_c < 3$). To mitigate some of the stray light effects the SHDOM results for clear sky ($\tau_c = 0$) are replaced by the measurements from the CSL for the rest of this analysis.

Figure 5d–f demonstrate USI images and a synthetic image from SHDOM for τ_c of 30. The cloud optical depth for input to SHDOM was determined from Min et al. (2003) measurements. The majority of the sky ($\vartheta_z < 80°$) red radiance differs by less than 5 %. At $\tau_c = 30$ direct normal irradiance (DNI) is absent and stray light can be neglected.

4 Impact of geometrical parameters and cloud optical depth on radiance and RBR

As described in Sect. 2, individual channel radiance and RBR are the most fundamental parameters for cloud detection in sky images. To obtain τ_c, the functions $I_\lambda(\tau_c)$ and $\mathrm{RBR}(\tau_c)$ must be parameterized. Furthermore, geometrical parameters (ϑ_z, ϑ_s) and solar position (θ_0) have been found to affect $\mathrm{RBR}(\tau_c)$ and $I_\lambda(\tau_c)$ (Shields et al., 1993) such that we must obtain $\mathrm{RBR}(\tau_c, \theta_0, \vartheta_s, \vartheta_z)$ and $I_\lambda(\tau_c, \theta_0, \vartheta_s, \vartheta_z)$ to solve the inverse problem. SHDOM enables us to analyze each of these parameters individually. In this section we will demonstrate how each variable affects I_λ and RBR.

4.1 Solar pixel angle

Figure 6a demonstrates for the red and blue channel that radiance decreases with increasing ϑ_s for non-thick clouds ($\tau_c < 30$). For thin clouds ($\tau_c = 1$) the radiance peaks in the solar region as a result of the forward scattering peak of the cloud phase function. As τ_c increases, radiance becomes constant with ϑ_s.

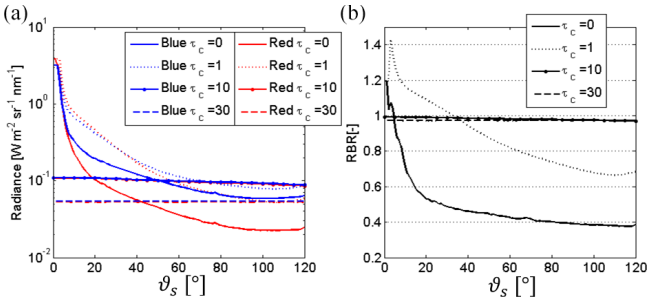

Figure 6. **(a)** SHDOM red and blue channel radiance over various sun pixel angles (ϑ_s) at $\vartheta_z = 60°$, and $\theta_0 = 60°$ (pixels used for Fig. 6 are highlighted as a red line in Fig. 3c). Results are shown for different cloud optical depths from clear ($\tau_c = 0$) to thick clouds. **(b)** RBR as a function of ϑ_s at constant $\vartheta_z = 60°$ and $\theta_0 = 60°$.

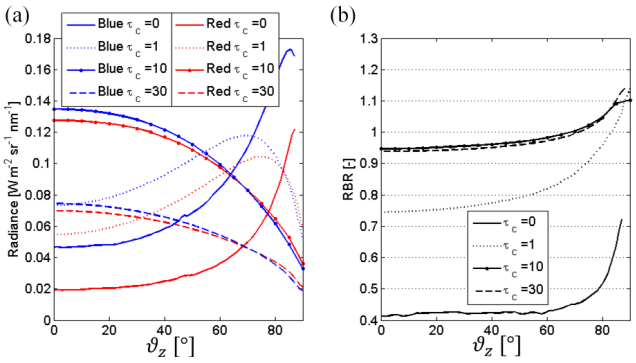

Figure 7. **(a)** Red and blue channel radiances and **(b)** RBR over various ϑ_z at constant $\vartheta_s = 60°$ and $\theta_0 = 60°$. Pixels used for Fig. 7 are highlighted as a red line in Fig. 3b.

Figure 6a shows that the blue radiance is larger than the red radiance under clear skies, except for very small ϑ_s, while for cloudy skies the two radiances are more similar. Therefore, most cloud detection methods assume that RBR is higher for clouds than for clear sky; however, Fig. 6b demonstrates that this is not always the case. At small ϑ_s ($\vartheta_s < 6°$) the RBR of thick clouds is lower than that of clear sky. Moreover, for $\tau_c = 1$ thin clouds have a higher RBR at $\vartheta_s < 30°$ than thick clouds. For $\tau_c <= 10$ RBR increases as ϑ_s approaches the solar region. At higher τ_c ($\tau_c >= 30$) RBR becomes constant over ϑ_s. Note that all of the statements in Sect. 4 strictly only apply for the θ_0 and ϑ_z shown in the figure, but Figs. 6–8 indicate that the conditions $\theta_0 = 60°$, $\vartheta_s = 60°$, and $\vartheta_z = 60°$ are representative for a wide range of conditions.

4.2 Sky imager zenith angle

Near the horizon (large ϑ_z), diffuse irradiance is commonly observed to be enhanced. Horizon brightening is indeed observed for clear skies in Fig. 7a. As clouds become thicker the dependence of radiance on ϑ_z is inverted and radiance decreases with increasing ϑ_z. The radiative transfer transitions into the diffusion regime, where it only depends on ϑ_z. In contrast, the RBR dependence has a similar shape independent of the τ_c (Fig. 7b). Pixels near zenith have lower RBR than those near the horizon.

4.3 Solar zenith angle

The effects of θ_0 are intuitive and consistent with what is observed during a sunset and therefore not graphically presented; the red and blue radiance is observed to decrease with increasing θ_0. The decrease in radiance is caused by the decrease in extraterrestrial horizontal flux as θ_0 increases. In contrast, RBR is found to increase with increasing θ_0, reflecting the increase in air mass with increasing θ_0. Increased air mass causes more blue light to be scattered back into space than red light.

4.4 Cloud optical depth

Figure 8a illustrates the ambiguity that arises when attempting to differentiate cloud optical depth with radiance. Radiance reaches a peak around $\tau_c = 3.25$ and almost for the entire range of τ_c the solution is not unique; i.e., there are two τ_c that lead to the same radiance. Figure 8b, however, demonstrates the ambiguity of τ_c detection using only RBR. SHDOM simulations demonstrate that as τ_c increases RBR increases until it reaches its maximum around $\tau_c = 2$ and then decreases until converging to a constant value for $\tau_c > 20$. This creates the following challenges: (i) RBR is insensitive to τ_c for $\tau_c > 20$ and therefore thick clouds of different τ_c cannot be distinguished and (ii) there is ambiguity because of the non-monotonic behavior. For example, clouds with a τ_c of 1.5 have similar RBR values to clouds of $\tau_c > 20$. While (outside the solar region, see Fig. 6b) RBR is a useful differentiator between clouds and clear sky, more information is needed to differentiate between different τ_c.

In addition, Fig. 8a highlights one of the main challenges of ground-based images compared to satellite-based cloud detection. In satellite-based τ_c detection, the measured radiance can be used to calculate τ_c (Nakajima and King, 1990) as the measured (upwelling) radiance monotonically increases with higher τ_c. This same method cannot be used for ground-based imagery as radiance increases for thin clouds peaks and then begins to decrease. This means that two τ_c can exist that produce the same radiance. It is again important to also note that the curves in Fig. 8 depend on ϑ_s and ϑ_z. For example, in the circumsolar ($\vartheta_s < 30°$) region red radiance peaks at $\tau_c \sim 0.75$ while clear sky has a higher radiance and higher RBR than thick clouds ($\tau_c > 5$). Approaching $\vartheta_z = 0°$ and far from the sun ($\vartheta_s > 60°$), the red radiance peaks at $\tau_c = 8.75$. Near the horizon ($\vartheta_z > 80°$) the red radiance peaks again at lower $\tau_c = 1.25$.

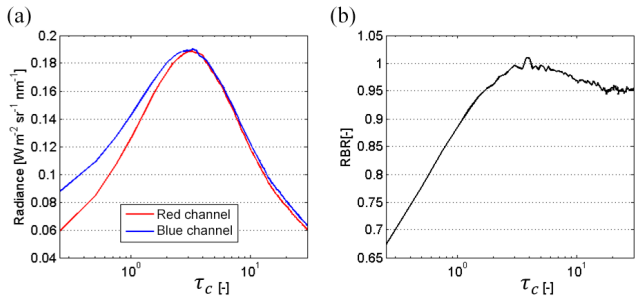

Figure 8. Red and blue channel radiance **(a)** and RBR **(b)** vs. τ_c for ϑ_s of 45°, θ_0 of 60°, and ϑ_z of 45°.

4.5 Expressing cloud optical depth through geometrical and solar parameters

Since it is currently computationally infeasible to use SHDOM to solve $\tau_c(I_\lambda, \mathrm{RBR}, \theta_0, \vartheta_s, \vartheta_z)$ in real time (~ 10 s) as required for sky imager solar forecasting, the homogeneous cases described in Sect. 3.1 are used instead to create interpolants. As seen in Fig. 8a and b, $\tau_c(I_\lambda, \theta_0, \vartheta_s, \vartheta_z)$ and $\tau_c(\mathrm{RBR}, \theta_0, \vartheta_s, \vartheta_z)$ are multivalued functions. Therefore two separate interpolants are created for each function. $\tau_c(I_\lambda, \theta_0, \vartheta_s, \vartheta_z)$ is split into τ_c that is higher than the peak radiance and τ_c that is lower than the peak radiance. $\tau_c(\mathrm{RBR}, \theta_0, \vartheta_s, \vartheta_z)$ is similarly split into τ_c that is higher than the peak RBR and τ_c that is lower than the peak RBR. Section 5 will describe how these interpolants are used to find up to two $\tau_c(I_\lambda^{\mathrm{meas}})$ (one for the higher and one for the lower branch of τ_c) and how a unique τ_c is obtained.

5 Radiance red–blue ratio (RRBR) method for cloud optical depth measurement

5.1 RRBR Algorithm

We have shown that it is difficult to distinguish between different τ_c by using RBR alone. As demonstrated in Fig. 8, radiance and RBR are non-monotonic functions of τ_c with generally two τ_c associated with the same radiance or RBR. However, for most cases, there is a unique τ_c solution for a pair of RBRs and radiance. The RRBR method attempts to obtain this solution by first solving $\tau_c(I_\lambda, \theta_0, \vartheta_s, \vartheta_z)$ and then substituting the (usually two) τ_c solutions into $\mathrm{RBR}(\tau_c, \theta_0, \vartheta_s, \vartheta_z)$ and identifying the correct τ_c as the one with the smallest $|\mathrm{RBR}^{\mathrm{meas}}(\theta_0, \vartheta_s, \vartheta_z) - \mathrm{RBR}(\tau_c, \theta_0, \vartheta_s, \vartheta_z)|$, where $\mathrm{RBR}^{\mathrm{meas}}(\theta_0, \vartheta_s, \vartheta_z)$ is the measured RBR. The algorithm for the RRBR method is depicted graphically in Fig. 9. I_λ at a wavelength of 620 nm is used because its variations with τ_c are larger than the other wavelengths. This larger dynamic range reduces the errors caused by instrument noise.

The algorithm begins by comparing $I_{620}^{\mathrm{meas}}(\theta_0, \vartheta_s, \vartheta_z)$ against $\max(I_{620}(\tau_c, \theta_0, \vartheta_s, \vartheta_z))$ (e.g., $0.19\,\mathrm{W\,m^{-2}\,sr^{-1}\,nm^{-1}}$ in Fig. 8a), where $I_{620}^{\mathrm{meas}}(\theta_0, \vartheta_s, \vartheta_z)$ is the measured radiance in the camera's red channel. Heterogeneity in clouds can cause $I_{620}^{\mathrm{meas}}(\theta_0, \vartheta_s, \vartheta_z)$ to be larger than $\max(I_{620}(\tau_c, \theta_0, \vartheta_s, \vartheta_z))$; in this case as the pixel conditions fall outside the range of the method the algorithm reverts back to τ_c assignment solely based on RBR and $\tau_c(\mathrm{RBR}, \theta_0, \vartheta_s, \vartheta_z)$ is used to find τ_c. If there are two solutions, then the τ_c associated with the maximum red radiance is used as there is no way to differentiate between the multiple solutions. Clouds brighter than the SHDOM radiance peak were found to only occur in 5.4 % of all pixels.

If $I_{620}^{\mathrm{meas}}(\theta_0, \vartheta_s, \vartheta_z)$ is within the range of $I_{620}(\tau_c, \theta_0, \vartheta_s, \vartheta_z)$, then τ_c is calculated from $\tau_c\left(I_{620}^{\mathrm{meas}}, \theta_0, \vartheta_s, \vartheta_z\right)$. If only one solution is found, the τ_c is assigned based on $\tau_c\left(I_{620}^{\mathrm{meas}}, \theta_0, \vartheta_s, \vartheta_z\right)$ and $\mathrm{RBR}(\tau_c, \theta_0, \vartheta_s, \vartheta_z)$ is not considered. When two solutions are found, they are input into $\mathrm{RBR}(\tau_c, \theta_0, \vartheta_s, \vartheta_z)$ and the one closest to $\mathrm{RBR}^{\mathrm{meas}}(\theta_0, \vartheta_s, \vartheta_z)$ is assigned.

An example τ_c estimate is presented in Fig. 10. The darker clouds (for example for the clouds between the sun and the horizon) are correctly identified as higher τ_c even though the RBR is lower than for the thinner clouds. In the circumsolar region, the RBR is largest but the RRBR method correctly identifies a thinner cloud. The black points in Fig. 10b corresponds to undetermined τ_c due to signal saturation. Since saturated pixel values near the sun exceed the dynamic range of the USI sensor, the RBR defaults to 1, the red radiance is unknown, and no τ_c can be assigned. In practice one could interpolate across the saturated region, but we prefer showing the raw results in this paper.

5.2 Impact of 3-D effects

Although the RRBR method is developed from overcast scenarios, we also apply this method to broken cloud scenes. The largest 3-D effect is the geometric difference in a broken cloud's optical path (τ_p) compared to an overcast cloud's τ_p (Hinkelman et al., 2007). Figure 11 illustrates the definition of τ_p as the optical thickness along the path of the direct solar beam, while τ_c is the optical thickness integrated along the vertical direction. For overcast clouds the τ_p is simply related to the τ_c as

$$\tau_c = \tau_p \cos(\theta_0). \tag{7}$$

However, for partial cloud cover the optical path changes along the cloud and as a result it affects I_λ, which in turn affects the RRBR retrieval. Ignoring horizontal photon transport, the RRBR's τ_c is then a function of the τ_p as in Eq. (7), which, unlike the actual τ_c, changes across the square cloud. Figure 12 demonstrates how the RRBR method retrieves τ_c for a 1 km × 1 km square cloud with a 0.2 km cloud geometric thickness. τ_c is observed to increase in the same way that τ_p increases. Therefore differences between the actual τ_c and the RRBR's τ_c will occur based on the geometry of the cloud.

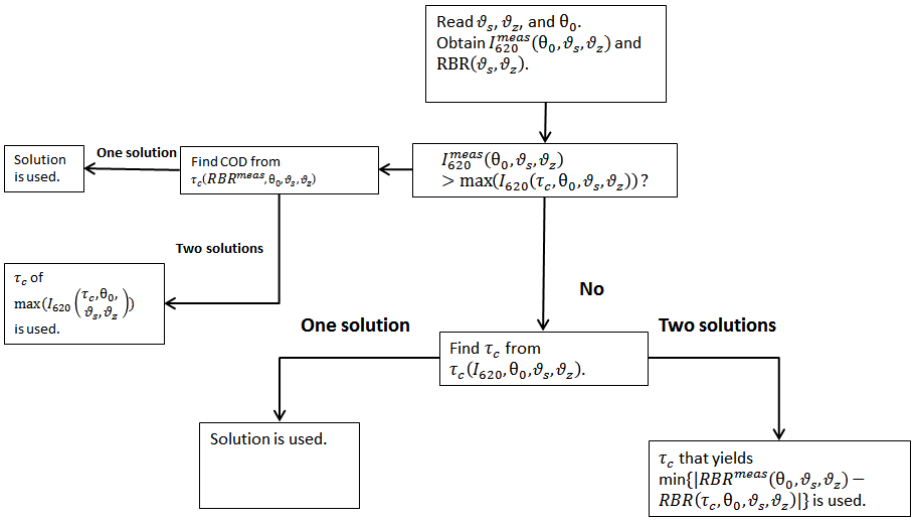

Figure 9. Flowchart of the radiance red–blue ratio (RRBR) method for τ_c estimation. If $I_{620}^{meas}(\theta_0, \vartheta_s, \vartheta_z)$ is saturated (e.g., in the solar disk), τ_c is assigned not-a-number.

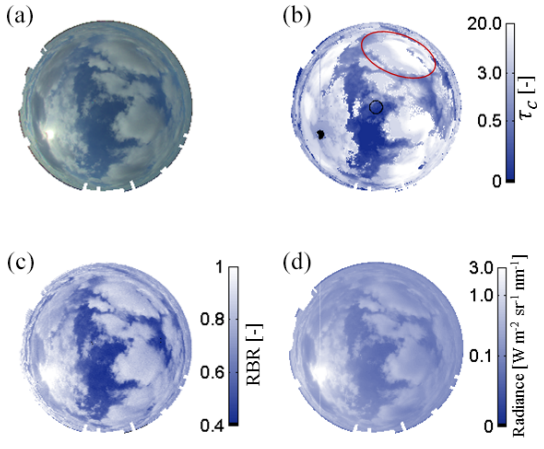

Figure 10. **(a)** USI image for 25 March 2013, 22:10:00 UTC. **(b)** τ_c retrieval from the RRBR method. Pixels inside the black ring are the pixels used for averaging and comparison with the MWR (Sect. 6.4). **(c)** RBR$^{meas}(\vartheta_s, \vartheta_z)$. **(d)** $I_{620}^{meas}(\theta_0, \vartheta_s, \vartheta_z)$. For this scene, the MWR measured a τ_c of 0.56 and the USI measured a τ_c of 0.20, the highest τ_c readings within 10 min of this image are 19.4 and 15.3 for the MWR and USI respectively.

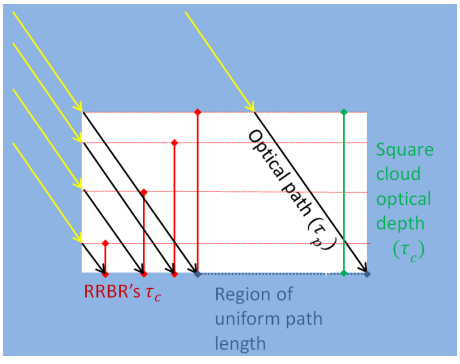

Figure 11. Illustration demonstrating differences between RRBR measured cloud optical depth, cloud optical depth, and cloud optical path.

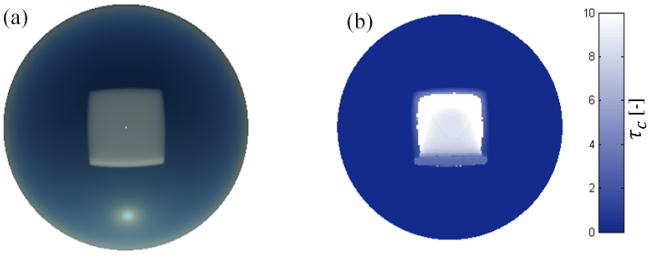

Figure 12. **(a)** SHDOM simulated sky image of a 1 km × 1 km square cloud with cloud geometric thickness of 0.2 km at a $\theta_0 = 60°$ and $\tau_c = 10$ **(b)** and RRBR τ_c retrieval. The RRBR τ_c is 8, 0.2 km from the cloud edge facing the sun.

Again ignoring horizontal photon transport, in ideal cases, such as a cubic cloud, the region of uniform path length where the actual τ_c and the RRBR's τ_c are similar is limited to $\theta_0 \ll 45°$. For square clouds with a small vertical extent, the region of uniform path length is increased, while for a square cloud of large vertical extent the region of uniform path length is decreased compared to the cubic cloud. For a parallelogram cloud aligned with the solar beam, the local homogeneity is extended to include most of the cloud base. The specifics of defining when clouds can be considered locally homogeneous will be left for future work. When horizontal photon transport is included it would be expected to decrease the area of homogeneity.

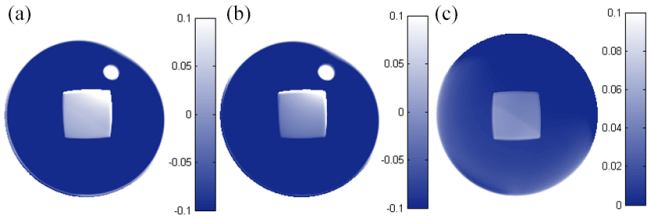

Figure 13. Relative difference in red radiance [–] between square and overcast clouds $(\frac{I^{\text{overcast}}_{\lambda=620} - I^{\text{square}}_{\lambda=620}}{I^{\text{overcast}}_{\lambda=620}})$ for surface reflectance **(a)** $R = 0.08$ and **(b)** $R = 0$; **(c)** difference between **(a)** and **(b)**, i.e., $((\frac{I^{\text{overcast}}_{\lambda=620} - I^{\text{square}}_{\lambda=620}}{I^{\text{overcast}}_{\lambda=620}})_{R=0.08} - (\frac{I^{\text{overcast}}_{\lambda=620} - I^{\text{square}}_{\lambda=620}}{I^{\text{overcast}}_{\lambda=620}})_{R=0})$.

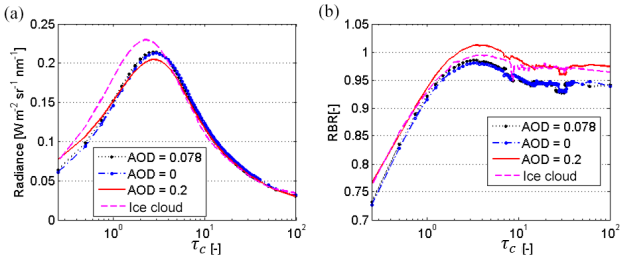

Figure 14. **(a)** Red radiance and **(b)** RBR for liquid clouds with $\tau_a = 0$, 0.078, and 0.2 and ice clouds with $\tau_a = 0.078$ vs. τ_c for $\vartheta_s = 45°$, $\theta_0 = 60°$, and $\vartheta_z = 45°$.

The second major 3-D effect is that heterogeneous clouds are brighter than homogeneous clouds under the same τ_c. This is caused by increased upwelling solar irradiance from the unshaded part of the scene, illuminating the cloud from below. The reflected light from the cloud underside increases brightness. This is demonstrated in Fig. 13 where overcast and square clouds were compared for two different spectral surface reflectances (R) for $\tau_c = 10$. The results demonstrate that the cloud bottom radiance increases 5 % due to a spectral surface reflectance of 0.08 at a wavelength of 620 nm. Adjusting the RRBR method to account for these effects is left for future work.

5.3 Impact of aerosols

The chosen τ_a is an additional source of error in the reference SHDOM simulations. Higher actual τ_a values than those in the simulations may lead to τ_a being classified as τ_c, while smaller τ_a lead to a reduced τ_c estimate. This error is small since most τ_c values are much larger than the variations in τ_a in the USA. Furthermore, this error is not important for solar forecasting as – spectral effects aside – only the total atmospheric optical depth is of interest to estimate ground irradiance, not the partition between τ_a and τ_c. As demonstrated in Fig. 14, variations in aerosol optical depth from 0 to 0.2 lead to changes in I_λ and RBR of less than 5 %.

The RRBR method was derived based on SHDOM results for a single layer liquid clouds but the model could be extended to ice clouds with additional SHDOM runs. Figure 14 demonstrates results from ice cloud simulations, with an effective radius of 100 µm. Ice clouds are not assessed in this paper as none of the methods used for comparison provide information for ice clouds. As for cloud scenes with multiple layers, the RRBR method represents the additive τ_c of all cloud layers.

6 Comparison

6.1 Other cloud optical depth measurements

The Min et al. (2003) method (Min and Harrison, 1996b; Min et al., 2003) is designed to estimate τ_c for conditions with homogenous clouds using the measured atmospheric transmittance of global radiation (also referred to as clearness index). The atmospheric transmittance is obtained using a multifilter rotating shadowband radiometer (MFRSR) as

$$T = \frac{\text{GHI}^{415\,\text{nm}}}{\text{GHI}_0^{415\,\text{nm}}}, \tag{8}$$

where $\text{GHI}^{415\,\text{nm}}$ is the global horizontal irradiance, and $\text{GHI}_0^{415\,\text{nm}}$ is the top of the atmosphere GHI, both at a wavelength of 415 nm. The MFRSR measurements at a wavelength of 415 nm is used in Eq. (8) to reduce effects of gaseous absorption. GHI_0 is adjusted from the true top-of-atmosphere GHI to remove τ_a influences on T, by applying Langley regression calibrations from the DNI on clear skies to the GHI (Harrison and Michalsky, 1994; Min and Harrison, 1996b). A discrete ordinate radiative transfer model is applied to identify the τ_c corresponding to the measured T (Min and Harrison, 1996a). By default a cloud effective radius (r_e) of 8 µm is assumed in the Min et al. (2003) method, but when liquid water path (LWP) values are available from a microwave radiometer (MWR), then r_e is solved iteratively. r_e is first solved for with Eq. (9) using LWP from the MWR and the Min et al. (2003) τ_c. Once obtained r_e is used as an input in the discrete ordinate model, which provides a different τ_c, which leads to a different r_e; this process is repeated until the changes in τ_c are below a threshold value. Min et al. concluded that the uncertainty in the inferred cloud properties caused by r_e was less than 5 %. Since the Min et al. method uses GHI measurements to estimate τ_c, the τ_c is representative of the sky hemisphere. At the ARM site the Min et al. (2003) τ_c is sampled and reported every 20 s. Since the Min et al. (2003) method only works for liquid clouds, only data with estimated cloud base temperature above 5° were used from the comparison dataset. The cloud base height is determined from ceilometer measurements and the cloud base temperature from the most recent sounding. Accurate τ_c is obtained with this method for $\tau_c > 10$, but for $\tau_c < 10$ the Min method is no longer valid (Turner et al., 2004).

A true validation requires independence of datasets. Due to the need to calibrate USI radiances, results from the Min method were required to develop the RRBR method for overcast conditions. Therefore, at least for overcast conditions, the datasets are not independent and we call it a comparison.

τ_c is also measured by an MWR. The MWR is a microwave receiver that detects the microwave emissions of the vapor and liquid water molecules. It measures cloud LWP in the zenith direction within a field of view of 6° (Liljegren, 2000; Cadeddu et al., 2013). τ_c can then be estimated as (Stephens, 1978)

$$\tau_c \approx \frac{\frac{3}{2}\int \mathrm{LWC}\,\mathrm{d}z}{\rho_l r_e} = \frac{\frac{3}{2}\mathrm{LWP}}{\rho_l r_e}, \quad (9)$$

where LWC is the cloud liquid water content and ρ_l is the density of liquid water. A r_e of 8 µm is assumed, as in the Min et al. method. The MWR has an irregular timestep ranging from 20 to 40 s. The uncertainty in the LWP obtained from the MWR is ±0.03 mm (30 g m^{-2}, Morris, 2006), which corresponds to a τ_c of ±5.6 with Eq. (8).

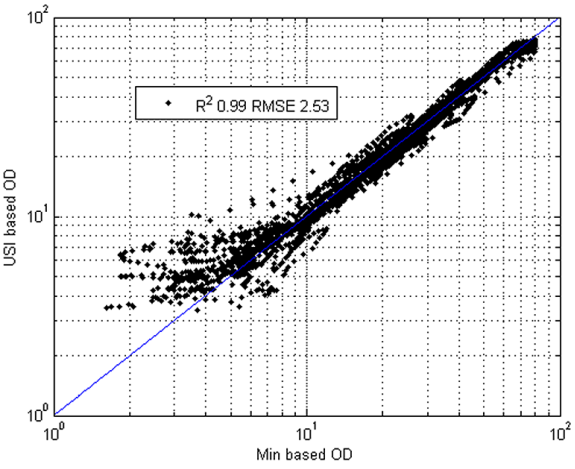

Figure 15. Comparison of RRBR τ_c retrievals from the sky imager vs. the Min et al. (2003) method applied to MFRSR measurements for USI cloud fractions greater than 0.7. USI results are averaged in irradiance space over the hemisphere as shown in Eq. (9).

6.2 Comparison in overcast conditions with Min algorithm

Data from the Min et al. (2003) algorithm are compared to the average τ_c from an entire USI image. Since the Min et al. (2003) method assumes overcast skies, only conditions with CF > 0.7 are used for this analysis yielding 5197 data points (about 43 h of data). The mean transmission of horizontally heterogeneous clouds is higher than the transmission of a uniform cloud with the same mean optical depth (Hinkelman et al., 2007). This is caused by the nonlinear relationship between τ_c and radiance.

To adjust the heterogeneous USI τ_c retrieval to be consistent with the Min et al. method, the USI τ_c was converted to irradiance for each pixel using a lookup table, averaged over the entire image in irradiance space, and then converted back to τ_c. Figure 15 compares results from both methods. An R^2 of 0.99 reflects the high correlation between the two methods. The relative RMSE decreases as τ_c increases as demonstrated in Table 2, with thin clouds ($\tau_c < 10$) having an RMSE of 27.2 % and thick clouds ($\tau_c > 30$) having an RMSE of 5.8 % with the overall RMSE being 8.2 %. RMSE at $\tau_c > 10$ is well below the 21 % required for solar energy applications (Fig. 1) and validates the RRBR method for thick overcast clouds ($\tau_c > 10$), but for $\tau_c < 10$ the Min et al. (2003) method is no longer valid (Turner et al., 2004) and the relative RMSE increases drastically. These differences in RMSE with τ_c highlight the difficulties in detecting thin clouds correctly.

Note that the zero mean bias error (MBE) between Min and RRBR for CF > 0.7 is partially a result of the cross-calibration in overcast conditions (because the cross-calibration data required CF > 0.95, the cross-calibration and validation data are different). However, the other errors between Min and RRBR in Table 2 are non-zero (i) because some of the data used for the comparison were not used for radiometric calibration, (ii) due to differences in the wavelengths of measurement (620 nm for RRBR and 450 nm for USI), and (iii) because radiation differences as USI use diffuse radiance while Min uses global irradiance to derive τ_c. Nevertheless the cross-calibration is expected to reduce the mean bias difference between Min and RRBR methods and the related error metrics are not representative of a truly independent dataset, especially for the CF > 0.7 scenario.

6.3 Heterogeneous and homogenous cloud conditions with the microwave radiometer

The RRBR method is compared to τ_c estimates from the MWR using the 12 422 pixels in each USI image with $\vartheta_z < 6°$. Figure 16 shows the comparison of the two methods. All conditions result in a RMSE of 3.6 or 19.0 % and R^2 of 0.98, again well within the minimum error requirement of 21 %. Since overcast data were already compared in Sect. 6.2, we now focus on cloud fractions of less than 0.7.

The RMSE is 2.23 for the heterogeneous cases, which is well within the uncertainty of the MWR measurements of ±5.6 but which corresponds to a relative RMSE of 85.0 % that exceeds the objectives set at the beginning. Just like in overcast conditions (Sect. 6.2), RMSE is highest for thin clouds ($\tau_c < 5$) at 71.7 %, decreases at medium cloud thickness ($10 < \tau_c < 30$) to 31.9 %, and increases once again for thick clouds ($\tau_c > 30$) to an RMSE of 56.8 %. The heterogeneous cases are associated with a higher relative RMSE of 85.0 % compared to 8.2 % reported in Sect. 6.2 for the homogeneous Min et al. (2003) method. The lower correlation of 0.66 between the two methods is probably related to (i) the uncertainty of the MWR, (ii) random errors in τ_c re-

Table 2. Statistics of RRBR comparison against the Min et al. method in overcast skies (cloud fraction > 0.7) and microwave radiometer (MWR) measurements. RMSE [–] is the absolute root mean square error, RMSE [%] is the relative root mean square error, MAE [%] is the relative mean average error, and MBE [%] is the relative mean bias error.

Method	CF	τ_c	R^2	RMSE [–]	RMSE [%]	MAE [%]	MBE [%]
Min	> 0.7	All	0.99	2.5	8.2	6.1	0.0
Min	> 0.7	< 10	0.55	1.6	27.2	20.6	12.1
Min	> 0.7	> 10 and < 30	0.88	1.8	9.3	7.2	−1.2
Min	> 0.7	> 30	0.97	3.4	5.8	4.5	−1.0
MWR	All	All	0.98	3.6	19.0	11.3	1.1
MWR	> 0.7	All	0.97	4.3	14.3	9.3	2.1
MWR	< 0.7	All	0.68	2.2	85.0	46.6	−14.4
MWR	< 0.7	< 10	0.58	1.5	71.7	49.9	−11.3
MWR	< 0.7	> 10 and < 30	0.42	4.5	31.9	24.6	−16.7
MWR	< 0.7	> 30	0.50	24.8	56.8	52.8	−52.8
Method	CF	τ_c	R^2	RMSE [–]	RMSE [%]	MAE [%]	MBE [%]

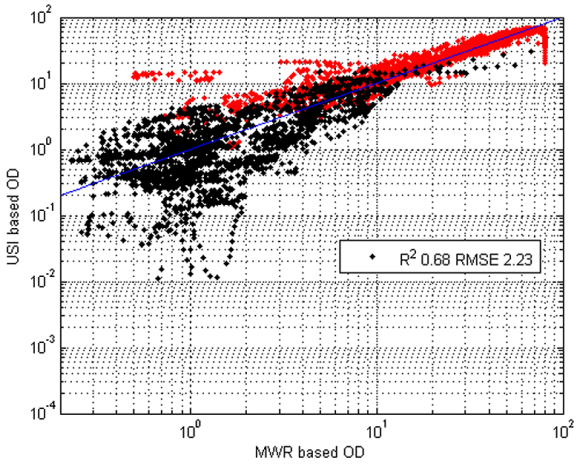

Figure 16. Comparison of USI RRBR vs. MWR measurements of cloud optical depth for CF < 0.7 in black and CF > 0.7 in red.

trievals under heterogeneous cloud conditions due to incomplete overlap of the field of view of the USI and MWR, (iii) 3-D cloud effects (Sect. 5.2), and (iv) uncertainty in the MWR τ_c related to the assumption of $r_e = 8\,\mu m$. Further research is needed to increase the correlation. While the SHDOM model calculations also assume constant r_e, this only affects the single scattering properties of the cloud – more specifically, the phase function. Consequently, the MWR algorithm is more sensitive to r_e as r_e errors are linearly proportional to MWR errors.

A MBE of −14.4 % is observed demonstrating a tendency for the RRBR method to underpredict τ_c. This can further be analyzed when MBE is split into τ_c categories. Thick clouds ($\tau_c > 30$) have the highest MBE of −52.8 % compared to thin clouds ($\tau_c < 10$) that have an MBE of −11.3 %. As described in Sect. 5.2 heterogeneous clouds are brighter than homogeneous clouds because of the reflected light from the ground surface, leading to higher radiance measurements and lower τ_c. Another factor that causes higher USI radiance measurements in heterogeneous clouds are cloud sides. Since clouds sides are no longer obscured such as those in overcast clouds, an increase in cloud illumination relative to overcast clouds increases radiance. For clouds that are thicker than the red radiance peak ($\tau_c = 7.25$) this increased radiance along the sun-facing edge of the cloud results in an underprediction of τ_c. The fact that MBE becomes more negative with increasing τ_c could be a result of neglecting 3-D effects in the RRBR method.

7 Discussion and conclusions

This paper presents an analysis of the atmospheric radiative transfer effects on sky imager cloud detection and retrieval of τ_c using synthetic images produced by the SHDOM. Synthetic images demonstrate that θ_0, τ_c, ϑ_s, and ϑ_z all significantly and often nonlinearly and non-monotonically affect radiance I_λ and RBR of sky image pixels. For thin clouds, $I_\lambda(\vartheta_s)$ increases rapidly as it approaches the sun, as a result of the strong forward peak in the cloud phase function. In contrast, for thick clouds $I_\lambda(\vartheta_s)$ is found to be near constant with solar pixel angle for $\tau_c > 30$. ϑ_z has two main effects: horizon brightening for thin clouds and horizon darkening for thick clouds. Thick clouds fall in the diffusion regime, where I_λ decreases with ϑ_z but is independent of other parameters.

At a ϑ_s of 45° $I_\lambda(\tau_c)$ is demonstrated to increase with increasing τ_c for thin clouds. It reaches a peak at a τ_c between 0 and 5, depending on ϑ_s and ϑ_z. At τ_c greater than 5, $I_\lambda(\tau_c)$ decreases with increasing τ_c. Similar characteristics are ob-

served for the RBR although it does not decrease as much after reaching its maximum, making it an effective tool for distinguishing between clear sky and thick clouds. However, neither $I_\lambda(\tau_c)$ nor $\mathrm{RBR}(\tau_c)$ are monotonic, leading to the difficulties in cloud detection and τ_c characterization with one parameter. The RRBR method combines the RBR and I_λ to overcome the non-monotonic nature of each individual parameter.

Summary statistics of the different comparisons are presented in Table 2. For overcast skies the RRBR yields τ_c that is consistent with the Min et al. (2003) method. For heterogeneous cloud fields ($\mathrm{CF} < 0.7$), comparisons with MWR measurements of LWC at zenith demonstrated that the RRBR method provides τ_c estimates with typical R^2 of 0.68 and RMSE of 2.2, which is well within the uncertainty of the MWR instrument (± 5.6), but more work needs to be done to validate that heterogeneous clouds are within the 21 % uncertainty required for solar applications. As demonstrated by the relative RMSE in Table 2, the RRBR method provides accurate τ_c for overcast thick clouds. The relative RMSE is larger for $\tau_c < 10$ for all comparison datasets and future development requires a new comparison method for thin clouds. These results validate the RRBR method for overcast clouds but consistent underpredictions of heterogeneous cloud optical depth require improvement in the method.

Characterizing the cloud heterogeneity effects may improve the RRBR method. As the RRBR method is based on interpolants developed from simulations of homogeneous overcast skies, cloud heterogeneity violates the assumptions and is likely the leading source of errors. Errors due to cloud heterogeneity have been analyzed mainly in the context of satellite remote sensing. Varnai (1998) and Chambers et al. (1997) observed that the cloud spatial reflectance variation is smoother than variations in τ_c. They hypothesized that optically thicker clouds would scatter more light to their thinner neighboring clouds, causing the thinner clouds to appear brighter and thicker (looking from space), while the thinner clouds would scatter less light to the thicker clouds, making them appear darker and thinner than expected for a homogeneous cloud scene. A similar but opposite effect is observed in ground-based imagery, where thicker clouds shade their neighboring thinner clouds, making them appear darker and thicker, but this effect is moderated by the location of the sun relative to the clouds. Figure 9 also shows that sun-facing cloud edges scatter more light, increasing I_λ and leading to thinner τ_c estimates than the cloud edges on the opposite side. Cloud edges facing away from the sun will be shaded by the rest of the cloud and will be estimated as being thicker. These 3-D effects introduce noise in RRBR estimations of τ_c. Although the comparison methods presented here are able to highlight some errors in the RRBR method no method was accurate enough to provide information about thin clouds ($\tau_c < 10$) and future development requires a new comparison method for thin clouds.

For solar applications, the pixel-by-pixel τ_c allows an estimate of the contribution of each individual pixel to the DNI, GHI, and diffuse horizontal irradiance at the surface. Solar forecasting will benefit in two ways. (i) Static fields of τ_c can be used to spatially modulate surface irradiance fields beyond the standard binary (clear – cloudy) solar irradiance, either in 1-D similar to Eq. (9) or using the homogeneous results from SHDOM simulations from a lookup table. (ii) Temporal evolution of τ_c can be used to extrapolate future cloud τ_c resulting from cloud dynamics. At present, τ_c is assumed to be steady as the cloud field is advected. An analysis of τ_c evolution especially for individual cumulus or stratocumulus clouds through a time series of the τ_c could improve solar forecast accuracy and extend forecast skill to longer forecast horizon. For example, stratocumulus clouds that tend to form overcast layers in coastal Southern California thin during the mornings and then break up rapidly over land. The RRBR can detect the cloud thinning rate and forecast breakup time.

8 Data availability

The raw image data used as input can be made available upon request to the corresponding author. In fact, he would be happy to provide any data from the ARM field trial from 11 March to 4 November 2013 from either or both camera systems that were deployed. (Each day, a single camera's imagery is about 3 GB and the request volume would have to be reasonable, e.g. for the 10 days cited.) However, it is expected that other authors interested in this paper would be users of their own sky imaging system and will likely want to perform the calibration on their own system.

The sky imagery data used in this work were collected as part of the UCSD Sky Imager Cloud Position Study (https://www.arm.gov/campaigns/sgp2013sicps) (Urquhart, 2013). Data from that study are available upon request to the corresponding author.

Appendix A

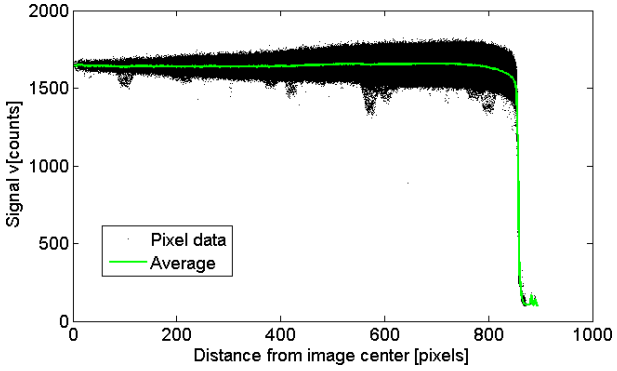

Figure A1. Uniformity of signal values vs. pixel distance from center, taken from 12 images with USI 1.7 under a Labsphere integrating sphere (LIS). In the LIS pixel signal should be homogeneous.

To adjust for errors due to an imperfect lens, the decrease of radiance in the radial direction (vignetting) was corrected by using measurements under an Labsphere integrating sphere (LIS). The LIS provides uniform light inside of the sphere. USI 1.7 was placed inside the LIS and images were taken. Figure A1 demonstrates the vignetting effects of a different USI that was deployed at ARM. Vignetting was corrected as

$$v_c = \frac{v_0}{v_x} v, \tag{A1}$$

where v is the original signal, v_c is the corrected signal, v_0 is the average signal value at the center of the uniform image, and v_x is the signal value of the uniform image at the pixel location being corrected. For USI1.7, $v_0 = 1645$ and v_x is the green line in Fig. A1.

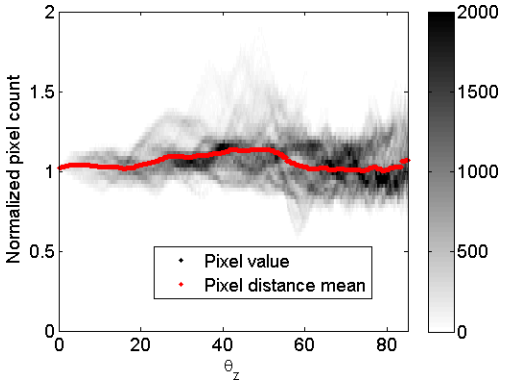

Figure A2. Pixel-by-pixel USI 1.7 signal for red, green, and blue divided by USI 1.8 signal (v_7/v_8 in Eq. 8) vs. sky imager zenith angle for an overcast sky. The grayscale shows the number of occurrences and the red line shows the mean. Since laboratory calibrations for USI 1.8 were not available, field data from an adjacent imager that was lab-calibrated (USI 1.7) were used to reduce vignetting for USI 1.8.

USI 1.7 vignetting was corrected directly using the LIS. Unfortunately USI 1.8 uses a slightly different setup and USI 1.8 was not available for LIS. Instead, USI 1.8 was corrected by comparing to USI 1.7 under a single overcast sky image at ARM as

$$v_c = \frac{v_7(\vartheta_z)}{v_8(\vartheta_z)} v(\vartheta_z). \tag{A2}$$

v_7 and v_8 are the signal of USIs 1.7 and 1.8 value under the overcast sky, respectively (Fig. A2).

Acknowledgements. Data were obtained from the Atmospheric Radiation Measurement (ARM) Program sponsored by the US Department of Energy, Office of Science, Office of Biological and Environmental Research, Climate and Environmental Sciences Division. We acknowledge funding from the CPUC California Solar Initiative RD&D program. The image data used in this experiment were collected during the UCSD Cloud Position Study, ARM Campaign 549. Felipe Mejia was supported by the National Science Foundation Graduate Research Fellowship under grant no. DGE-1144086. Bryan Urquhart is thanked for managing the ARM campaign.

Edited by: B. Mayer
Reviewed by: three anonymous referees

References

Cadeddu, M. P., Liljegren, J. C., and Turner, D. D.: The Atmospheric radiation measurement (ARM) program network of microwave radiometers: instrumentation, data, and retrievals, Atmos. Meas. Tech., 6, 2359–2372, doi:10.5194/amt-6-2359-2013, 2013.

Cahalan, R. F., Oreopoulos, L., Marshak, A., Evans, K. F., Davis, A. B., Pincus, R., Yetzer, K. H., Mayer, B., Davies, R., and Ackerman, T. P.: The 13RC-Bringing together the most advanced radiative transfer tools for cloudy atmospheres, B. Am. Meteorol. Soc., 86, 1275–1293, 2005.

Calbo, J. and Sabburg, J.: Feature extraction from whole-sky ground-based images for cloud-type recognition, J. Atmos. Ocean. Tech., 25, 3–14, 2008.

Cazorla, A., Olmo, F. J., and Alados-Arboledas, L.: Development of a sky imager for cloud cover assessment, J. Opt. Soc. Am. A, 25, 29–39, 2008.

Chambers, L. H., Wielicki, B. A., and Evans, K. F.: Accuracy of the independent pixel approximation for satellite estimates of oceanic boundary layer cloud optical depth, J. Geophys. Res.-Atmos., 102, 1779–1794, 1997.

Chow, C. W., Urquhart, B., Lave, M., Dominguez, A., Kleissl, J., Shields, J., and Washom, B.: Intra-hour forecasting with a total sky imager at the UC San Diego solar energy testbed, Sol. Energy, 85, 2881–2893, 2011.

Evans, K. F.: The spherical harmonics discrete ordinate method for three-dimensional atmospheric radiative transfer, J. Atmos. Sci., 55, 429–446, 1998.

Gauchet, C., Blanc, P., Espinar, B., Charbonnier, B., and Demengel, D.: Surface solar irradiance estimation with low-cost fisheye camera, in: Workshop on "Remote Sensing Measurements for Renewable Energy", May 2012.

Ghonima, M. S., Urquhart, B., Chow, C. W., Shields, J. E., Cazorla, A., and Kleissl, J.: A method for cloud detection and opacity classification based on ground based sky imagery, Atmos. Meas. Tech., 5, 2881–2892, doi:10.5194/amt-5-2881-2012, 2012.

Hammer, A., Heinemann, D., Lorenz, E., and Lückehe, B.: Short-term forecasting of solar radiation: a statistical approach using satellite data, Sol. Energy, 67, 139–150, 1999.

Harrison, L. and Michalsky, J.: Objective algorithms for the retrieval of optical depths from ground-based measurements, Appl. Opt., 33, 5126–5132, 1994.

Heinle, A., Macke, A., and Srivastav, A.: Automatic cloud classification of whole sky images, Atmos. Meas. Tech., 3, 557–567, doi:10.5194/amt-3-557-2010, 2010.

Hinkelman, L. M., Evans, K. F., Clothiaux, E. E., Ackerman, T. P., and Stackhouse Jr., P. W.: The effect of cumulus cloud field anisotropy on domain-averaged solar fluxes and atmospheric heating rates, J. Atmos. Sci., 64, 3499–3520, 2007.

Holben, B., Eck, T., Slutsker, I., Tanre, D., Buis, J., Setzer, A., Vermote, E., Reagan, J., Kaufman, Y., and Nakajima, T.: AERONET – A federated instrument network and data archive for aerosol characterization, Remote Sens. Environ., 66, 1–16, 1998.

Holben, B., Tanre, D., Smirnov, A., Eck, T., Slutsker, I., Abuhassan, N., Newcomb, W., Schafer, J., Chatenet, B., and Lavenu, F.: An emerging ground-based aerosol climatology: Aerosol optical depth from AERONET, J. Geophys. Res.-Atmos., 106, 12067–12097, 2001.

Kassianov, E., Long, C. N., and Christy, J.: Cloud-base-height estimation from paired ground-based hemispherical observations, J. Appl. Meteorol., 44, 1221–1233, 2005.

Kegelmeyer Jr., W.: Extraction of cloud statistics from whole sky imaging cameras, No. SAND–94-8222, Sandia National Labs., Livermore, CA, USA, 1994.

Koehler, T., Johnson, R., and Shields, J.: Status of the whole sky imager database, in: Proc. Cloud Impacts on DOD Operations and Systems Conference, El Segundo, CA, Department of Defense, 77–80, 1991.

Liljegren, J. C.: Automatic self-calibration of ARM microwave radiometers, in: Microwave Radiometry and Remote Sensing of the Environment, edited by: Pampaloni, P., VSP Press, Boston, MA, 433–441, 2000.

Long, C. N., Sabburg, J. M., Calbó, J., and Pagès, D.: Retrieving cloud characteristics from ground-based daytime color all-sky images, J. Atmos. Ocean. Tech., 23, 633–652, 2006.

Lorenz, E., Hurka, J., Heinemann, D., and Beyer, H. G.: Irradiance forecasting for the power prediction of grid-connected photovoltaic systems, IEEE J. Sel. Top. Appl., 2, 2–10, 2009.

Mantelli Neto, S. L., von Wangenheim, A., Pereira, E. B., and Comunello, E.: The use of Euclidean geometric distance on RGB color space for the classification of sky and cloud patterns, J. Atmos. Ocean. Tech., 27, 1504–1517, 2010.

Marchand, R. and Ackerman, T.: Evaluation of radiometric measurements from the NASA Multiangle Imaging Spectroradiometer (MISR): Two-and three-dimensional radiative transfer modeling of an inhomogeneous stratocumulus cloud deck, J. Geophys. Res.-Atmos., 109, D18208, doi:10.1029/2004JD004710, 2004.

Marshak, A. and Davis, A.: 3D radiative transfer in cloudy atmospheres, Springer Science & Business Media, Springer, New York, 2005.

Martínez-Chico, M., Batlles, F., and Bosch, J.: Cloud classification in a mediterranean location using radiation data and sky images, Energy, 36, 4055–4062, 2011.

Mathiesen, P. and Kleissl, J.: Evaluation of numerical weather prediction for intra-day solar forecasting in the continental United States, Sol. Energy, 85, 967–977, 2011.

Mathiesen, P., Collier, C., and Kleissl, J.: Case Studies with the Weather and Research Forecasting Model at GL-Garrad Hassan, in: Solar Resource Assessment and Forecasting, 1st edition, edited by: Kleissl, J., Elsevier, 358–381, Boston, 2013.

McGuffe, K. and Henderson-Sellers, A.: Almost a century of "imaging" clouds over the whole-sky dome, B. Am. Meteorol. Soc., 70, 1243–1253, 1989.

Min, Q. and Harrison, L. C.: An adjoint formulation of the radiative transfer method, J. Geophys. Res.-Atmos., 101, 1635–1640, 1996a.

Min, Q. and Harrison, L. C.: Cloud properties derived from surface MFRSR measurements and comparison with GOES results at the ARM SGP Site, Geophys. Res. Lett., 23, 1641–1644, 1996b.

Min, Q., Duan, M., and Marchand, R.: Validation of surface retrieved cloud optical properties with in situ measurements at the Atmospheric Radiation Measurement Program (ARM) South Great Plains site, J. Geophys. Res.-Atmos., 108, 4547, doi:10.1029/2003JD003385, 2003.

Miyamoto, K.: Fish eye lens, J. Opt. Soc. Am., 54, 1060–1061, 1964.

Morris, V.: Microwave radiometer (mwr) handbook, Tech. Rep. ARM TR-016, US Department of Energy, Argonne, IL, 2006.

Nakajima, T. and King, M. D.: Determination of the optical thickness and effective particle radius of clouds from reflected solar radiation measurements. Part I: Theory, J. Atmos. Sci., 47, 1878–1893, 1990.

Pfister, G., McKenzie, R. L., Liley, J. B., Thomas, A., Forgan, B. W., and Long, C. N.: Cloud coverage based on all-sky imaging and its impact on surface solar irradiance, J. Appl. Meteorol., 42, 1421–1434, 2003.

Pincus, R. and Evans, K. F.: Computational cost and accuracy in calculating three-dimensional radiative transfer: Results for new implementations of Monte Carlo and SHDOM, J. Atmos. Sci., 66, 3131–3146, 2009.

Román, R., Antón, M., Cazorla, A., de Miguel, A., Olmo, F. J., Bilbao, J., and Alados-Arboledas, L.: Calibration of an all-sky camera for obtaining sky radiance at three wavelengths, Atmos. Meas. Tech., 5, 2013–2024, doi:10.5194/amt-5-2013-2012, 2012.

Roy, G., Hayman, S., and Julian, W.: Sky analysis from CCD images: cloud cover, Lighting Research and Technology, 33, 211–221, 2001.

Seiz, G., Shields, J., Feister, U., Baltsavias, E., and Gruen, A.: Cloud mapping with ground-based photogrammetric cameras, Int. J. Remote Sens., 28, 2001–2032, 2007.

Shields, J., Johnson, R., and Koehler, T.: Automated whole sky imaging systems for cloud field assessment, in: Fourth Symposium on Global Change Studies, American Meteorological Society, 17–22 January 1993.

Souza-Echer, M., Pereira, E., Bins, L., and Andrade, M.: A simple method for the assessment of the cloud cover state in high-latitude regions by a ground-based digital camera, J. Atmos. Ocean. Tech., 23, 437–447, 2006.

Stephens, G.: Radiation profiles in extended water clouds. II: Parameterization schemes, J. Atmos. Sci., 35, 2123–2132, 1978.

Szczodrak, M., Austin, P. H., and Krummel, P.: Variability of optical depth and effective radius in marine stratocumulus clouds, J. Atmos. Sci., 58, 2912–2926, 2001.

Turner, D. D., Lo, C., and Min, Q.: Cloud Optical Properties from the Multi-Filter Shadowband Radiometer (MFRSRCLDOD): An ARM Value-Added Product, Pacific Northwest National Laboratory, ARM TR-047, 13 pp., 2004.

Urquhart, B.: Campaign: UCSD Sky Imager Cloud Position Study, available at: https://www.arm.gov/campaigns/sgp2013sicps, 2013.

Urquhart, B., Ghonima, M., Dung, A., Kurtz, B., Chow, C. W., and Kleissl, J.: Sky Imaging Systems for Short-term Forecasting, in: Solar Resource Assessment and Forecasting, 1st Edition, edited by: Kleissl, J., Elsevier, Boston, MA, 196–229, 2013.

Urquhart, B., Kurtz, B., Dahlin, E., Ghonima, M., Shields, J. E., and Kleissl, J.: Development of a sky imaging system for short-term solar power forecasting, Atmos. Meas. Tech., 8, 875–890, doi:10.5194/amt-8-875-2015, 2015.

Varnai, T.: Influence of Three-Dimensional Radiative Effects on the Spatial Distribution of Shortwave Cloud Reflection, J. Atmos. Sci., 57, 216–227, 1998.